

Reducing Entanglement With Physically-Inspired Fermion-To-Qubit Mappings

Teodor Parella-Dilmé,¹ Korbinian Kottmann,¹ Leonardo Zambrano,¹
Luke Mortimer,¹ Jakob S. Kottmann,² and Antonio Acín^{1,3}

¹*ICFO - Institut de Ciències Fotoniques, The Barcelona Institute of Science and Technology,
Av. Carl Friedrich Gauss 3, 08860 Castelldefels (Barcelona), Spain*

²*Institute for Computer Science, University of Augsburg, Germany*

³*ICREA-Institució Catalana de Recerca i Estudis Avançats, Lluís Companys 23, 08010 Barcelona, Spain*

(Dated: November 14, 2023)

In ab-initio electronic structure simulations, fermion-to-qubit mappings represent the initial encoding step of the fermionic problem into qubits. This work introduces a physically-inspired method for constructing mappings that significantly simplify entanglement requirements when simulating states of interest. The presence of electronic excitations drives the construction of our mappings, reducing correlations for target states in the qubit space. To benchmark our method, we simulate ground states of small molecules and observe an enhanced performance when compared to classical and quantum variational approaches from prior research employing conventional mappings. In particular, on the quantum side, our mappings require a reduced number of entangling layers to achieve chemical accuracy for the LiH , H_2 , $(H_2)_2$ and H_4 molecules using the RY hardware efficient ansatz. In addition, our mappings also provide an enhanced ground state simulation performance in the density matrix renormalization group algorithm for the N_2 molecule.

I. INTRODUCTION

Electronic structure ab-initio quantum chemistry simulations play a pivotal role in various fields, including drug development [1, 2], computational catalysis [3], and material science [4]. Given the significance of this domain, numerous techniques have evolved over the years, enabling simulations of increasingly complex systems. In the context of our research, it is worth mentioning three specific methodologies: classical simulations, variational quantum algorithms executed on current and near-term noisy quantum devices, and fault-tolerant quantum computing. Classical simulations, in form of the density matrix renormalization group algorithm (DMRG) [5–8] and Monte-Carlo methods [9], stand as state of the art methodologies and are readily available. Variational quantum algorithms are executed on proof-of-concept scales on contemporary noisy quantum computing devices, and hold the potential to achieve simulations of useful system sizes in the near future. Finally, quantum algorithms on fault tolerant quantum computers are projected to yield useful applications in a farther future where such computers are available, and the gate counts and runtimes of these algorithms reduced to practical numbers.

Central to all three approaches is the transformation of the physical problem into units of information. This involves the selection of an appropriate basis consisting in a set of spin-orbitals (SOs), on top of a fermion-to-qubit mapping. In this work, we focus on the choice of fermion-to-qubit mappings, which leads to potential advantages in all three formerly mentioned avenues.

Fermion-to-qubit mappings represent the initial encoding step of fermionic problems into qubits, faithfully

replicating the algebra of fermionic operators on a qubit system [10]. Given the non-local nature of the fermionic state space, these mappings introduce a non-local structure into qubit systems, which are typically characterized by a limited connectivity. It is crucial to emphasize that these mappings are not unique, as there are numerous possible solutions to the encoding problem. Consequently, depending on the qubit topology and the applied technique, some mappings may prove more advantageous than others for simulation tasks. In this context, the reduction of Pauli weight, mapped operators locality, entangling gate overhead and number of qubits has played a leading role in the design of novel mappings, all while considering the practical constraints imposed by experimental hardware [11–17]. Here, we follow a different path and choose entanglement as the relevant figure of merit: our goal is to design fermion-to-qubit mappings that reduce the entanglement in the target qubit state.

Given an initial fermionic Hamiltonian, its energy spectrum remains invariant under any valid fermion-to-qubit transformation. However, the eigenstates of the resulting qubit Hamiltonian, and consequently, the target state $|\psi\rangle$ to be simulated, differs across the mappings. In particular, it can exhibit substantial variations on its entanglement properties in qubit representation, which is a critical factor influencing the quality of the simulations, both in the classical and quantum case. For instance, it is not clear if the Pauli weight has any impact on DMRG simulations, while they are known to be affected by the entanglement structure of the target state. In general, identifying mappings yielding to states with reduced entanglement requirements could substantially enhance simulation performance.

In this work, a physically-inspired method is proposed to

construct tailored entanglement-aware fermion-to-qubit mappings with reduced entanglement requirements on the state being simulated. For small molecular systems, we prove enhanced ground-state preparation performance respect to paradigmatic mappings, both in the quantum computation framework using the variational quantum eigensolver (VQE), and in the tensor networks framework using the DMRG on a matrix product state (MPS) representation.

II. FERMION-TO-QUBIT MAPPINGS

The problem of designing beneficial qubit representations of electronic systems is rich and can be tackled from different angles. As mentioned, in this work we are focusing on the fermion-to-qubit mapping alone. Other works employ different strategies to reach this goal, such as optimizing the spatial orbitals [18–20], or regularizing the electronic Hamiltonian [21–27]. Note that these are separate strategies that can be combined with optimized fermion-to-qubit mappings.

The proposed mappings can be related to recent works aiming to find optimal Clifford circuits for entanglement reduction [28–30]. These works can be interpreted as finding a beneficial mapping through a transformation included in the quantum circuit, while in this work we aim to find a suitable mapping directly. Our results therefore apply to both classical and quantum approaches.

A. Fock Space to Qubits

The antisymmetrized Fock space \mathcal{F}_- encompasses all conceivable states from a many-body fermionic system. In electronic structure problems, solving for the spectrum of an operator $\hat{O} \in \text{Lin}[\mathcal{F}_-]$ holds significant importance, a particular case being the electronic Hamiltonian. The fermionic algebra consists in a set of creation $\{a_i^\dagger\}_{i=1}^n$ and annihilation $\{a_i\}_{i=1}^n$ operators in $\text{Lin}[\mathcal{F}_-]$, satisfying Canonical Anticommutation Relations (CAR):

$$\{a_i^\dagger, a_j\} = \delta_{ij} \mathbb{1} \quad , \quad \{a_i, a_j\} = \{a_i^\dagger, a_i^\dagger\} = 0 \quad . \quad (1)$$

When applied to the fermionic vacuum $|vac\rangle$, such ladder operators define the orthonormal Fock basis spanning \mathcal{F}_- , in the so-called occupation number vectors notation

$$|f_1, f_2, \dots, f_n\rangle \equiv (a_1^\dagger)^{f_1} (a_2^\dagger)^{f_2} \dots (a_n^\dagger)^{f_n} |vac\rangle \quad . \quad (2)$$

Here, $f_i \in \{0, 1\}$ is called the fermionic occupation of mode i , $(a_i^\dagger)^0 \equiv \mathbb{1}$ and n is the total number of fermionic modes available. Note that the ladder operators are applied in descending order, as a phase factor could apply

otherwise. Equivalently, ladder operators can be decomposed as

$$a_j = \frac{1}{2}(\gamma_{2j} + i\gamma_{2j-1}) \quad , \quad a_j^\dagger = \frac{1}{2}(\gamma_{2j} - i\gamma_{2j-1}) \quad , \quad (3)$$

into a self-adjoint part (γ_{2j}) and an anti-self-adjoint part $(i\gamma_{2j-1})$. They are uniquely identified by a Majorana basis $\{\gamma_j\}_{j=1}^{2d}$, satisfying both being self-adjoint ($\gamma_j = \gamma_j^\dagger$) and the associated CAR for Majoranas

$$\{\gamma_j, \gamma_k\} = 2\delta_{jk} \mathbb{1} \quad . \quad (4)$$

Operators in $\text{Lin}[\mathcal{F}_-]$ can be expressed as linear combinations of products of a set of ladder operators. In particular, the electronic Hamiltonian is expressed as a linear combination of one-body and two-body operators as

$$\hat{H}_e = \sum_{i,j} h_{ij} \hat{a}_i^\dagger \hat{a}_j + \sum_{i,j,k,l} h_{ijkl} \hat{a}_i^\dagger \hat{a}_j^\dagger \hat{a}_l \hat{a}_k \quad , \quad (5)$$

with h_{ij} , h_{ijkl} as the one and two-body terms respectively, available from classical computation methods.

The abstract Fock space spanned by n fermionic modes is isomorphic to the Hilbert space spanned by n qubits $\mathcal{F}_- \simeq (\mathbb{C}^2)^{\otimes n}$, with dimension 2^n . Hence, it is always possible to transform the Fock space to a qubit space through a so-called fermion-to-qubit mapping:

$$\Lambda : \quad \mathcal{F}_- \rightarrow (\mathbb{C}^2)^{\otimes n} \quad . \quad (6)$$

These mappings also transform ladder operators into operators in $\text{Lin}[\mathcal{F}_-]$ satisfying the CAR. After application of any of such mappings, any electronic Hamiltonian \hat{H}_e is fully reconstructed in the qubit space.

B. Ternary Tree Encodings

Ternary tree (TT) mappings were initially introduced [11] to minimise the Pauli weight of those operators in $\text{Lin}[\mathcal{F}_-]$ associated to fermionic operators, that is, to derive Pauli strings acting on the least amount of qubits. This ignited the research in [17], where a general TT formalism was constructed. It provides a large framework of fermion-to-qubit mappings based on Pauli strings, including the representation of traditional mappings such as Jordan-Wigner (JW) [31], Parity and Fenwick tree based mappings like Bravyi-Kitaev [10]. Such TT formalism enables the retrieval of a Majorana basis set in the qubit representation from a TT, satisfying Eq.(4). Moreover, it provides the string pairing conditions that guarantee the simplicity of the mapped vacuum and Fock basis states, on top of occupation localisation analysis.

We briefly introduce a TT as a graph $\mathcal{T} = (V, E)$ consisting of a set of m vertices $V = \{v_i\}_{i=1}^m$ and $(m-1)$

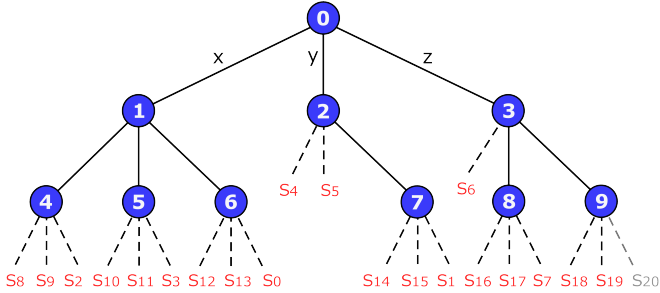


Figure 1. Ternary Tree example, corresponding to a fermion-to-qubit mapping of 10 fermionic modes. Each node holds a fermionic mode, an ascending parent node (except from the root node at the top), and three descending labeled branches x, y, z (from left to right respectively) indicating the child nodes. The dashed lines correspond to legs of the tree, each retrieving a single Majorana string S_i in red. The leg associated to z -paths form the root node is marked in grey, and its Majorana string is unpaired.

connecting edges $E \subseteq \{(x, y) \in V^2 | x \neq y\}$ [Fig.1]. In the upper part of the TT there is the root node, which ramifies the graph iteratively up to 3 labeled descendants per node. For two connected nodes v_i, v_j , a kinship relationship is set between them. With respect to v_i , the node v_j can take the relationship of parent (v_i^p), x -child (v_i^x), y -child (v_i^y) or z -child (v_i^z). The same applies for v_i . Except for the root node (which has no parent), every node has one and only one associated parent, and up to three labeled children. If a node is missing some x, y or z child, then for each missing child a leg from the ternary tree is defined. In total, there are $2m + 1$ resulting legs on the ternary tree. Each leg l has an associated Pauli string S_l , which can be retrieved by tracing the ascending path back to the root node. First, the node v_i on top of the leg $x/y/z$ implies an $X/Y/Z$ Pauli operator to be applied on the i th qubit. This step is repeated for the upcoming parent node $v_j = v_i^p$, tensoring the corresponding Pauli operator to qubit j depending on the TT label. The process is repeated until achieving the root node. The retrieved Pauli strings are in fact Majorana strings, satisfying Eq.(4). Ultimately, the Majorana strings are paired in order to preserve the fermionic vacuum through the pairing algorithm [Alg.2] in the appendix.

For further details about the TT formalism, we refer the reader to the detailed explanation in [17]. In this work, the TT formalism has been implemented using the TEQUILA [32] Python library.

C. Fermionic Permutation and Qubit Permutation

In this section, our aim is to discuss a fundamental yet often misunderstood distinction between fermionic permutation and qubit permutation. The former refers to the relative permutation of fermionic modes encoded

within the TT mapping, directly affecting the transformation and further simulation requirements [33]. The latter involves a reordering of qubits, leaving the transformation intact but bearing significant implications when conducting simulations with algorithms or devices with restricted topologies. To ensure clarity, we elaborate on the distinction between both permutations through explicit and illustrative examples.

We draw special attention to the resulting effects of encoding parity locally. In the literature, parity mappings are often referred to as a unique parity mapping. However, the specific order in which the fermionic occupation is encoded results in non-equivalent mappings.

Encoding locally in parity involves encoding in either the x -branch or the y -branch of a ternary tree. To simplify our discussion, we will focus on the former case and consider an x -branch mapping of 4 fermionic modes labeled 0,1,2,3, onto four qubits labeled A,B,C,D in standard order [Fig.2a]. We will explore another x -branch parity mapping where modes are encoded in the order 1,3,0,2 [Fig.2b]. Lastly, we present the JW mapping in the standard order for the purpose of comparison [Fig.2c].

The fermionic modes held by each node from the tree do have relevant implications on the mapping, and do in fact lead to different fermion-to-qubit mappings. We say that the two parity mappings presented differ due to a permutation in the fermionic space. Considering the first mapping [Fig.2a], qubit D holds the occupation of fermionic mode 3, qubit C the total occupation sum modulo 2 of modes 2 and 3, qubit B the total occupation sum modulo 2 of modes 1,2 and 3, and qubit A the total occupation sum modulo 2 of all 4 modes. However, in the case of mapping [Fig.2b], qubit D holds the occupation of fermionic mode 2, qubit C the occupation modulo 2 of modes 0 and 2, qubit B the occupation modulo 2 of modes 3, 0 and 2, and qubit A the occupation modulo 2 of all 4 modes. Both mappings have qubits that encode different occupation information from any other qubit in the other mapping. For instance, in the first mapping there is a qubit holding occupation information from mode 3, or a qubit holding occupation modulo 2 of modes 2 and 3. However, in the second parity mapping there are no such qubits, instead they are different. They are essentially non-equivalent fermion-to-qubit mappings, leading to alternative representations of the Fock space in the qubit space.

On top of this fermionic permutation that changes the mapping, one can define the physical qubit permutation, related to the relative order of the qubits A,B,C,D. Such physical permutation matters when the order of entangled subparties is relevant within an optimization method. For instance, physical permutation is important within a VQE optimization in a device with restricted qubit connectivity, or in a specific topological decompo-

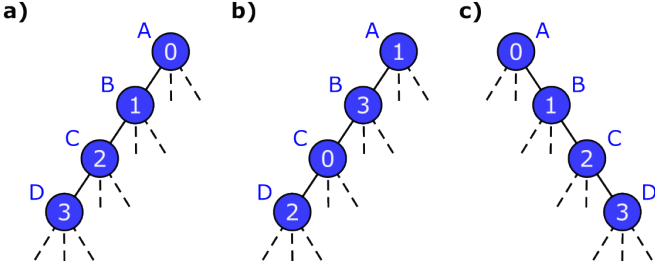


Figure 2. Ternary trees of fermion-to-qubit encodings with 4 fermionic modes (0,1,2,3) into 4 qubits (A,B,C,D). **a)** Parity encoding of fermions in standard order (0,1,2,3). **b)** Parity encoding of permuted fermions in order (1,3,0,2). **c)** JW encoding in standard order.

sition of a tensor (such as in a linear MPS). We remark that the physical permutation does not modify the representation of a state, but it has implications on optimization methods with finite resources.

III. SIMPLIFYING ENTANGLEMENT BY ENCODING OCUPATION NON-LOCALLY

The study of many-body electronic ground states involves dealing with complex correlations. Typically, a Hartree-Fock (HF) self-consistent field approach is used in first instance to identify an optimized separable state. However, to account for correlations, it is essential to consider electronic excitations, which entail promoting electrons from occupied SOs to virtual ones. Currently, widely-used methods like configuration interaction [34] and coupled cluster [35] aim to represent these excitations through parameterizations. The principle remains similar in its unitary variant (UCC) (see section IV) [36].

In this section, we propose an approach to streamline the treatment of correlations during the fermion-to-qubit encoding process. To illustrate this idea, we initially examine idealized fermionic scenarios involving pure states.

A. Double electronic excitation

We first consider a scenario involving four SOs related to a double excitation, which corresponds to the simultaneous promotion of two electrons. In the context of the JW encoding [Fig.2c], the occupation information of the initially-filled fermionic modes 0 and 1 is locally encoded in qubits A and B respectively. Similarly, the occupation of the two virtual fermionic modes 2 and 3 is locally encoded in qubits C and D. In this context, the state resulting from the double excitation is represented as follows:

$$|\psi\rangle_{ABCD}^{JW} = \alpha|1100\rangle_{ABCD}^{JW} + \beta|0011\rangle_{ABCD}^{JW} . \quad (7)$$

An alternative approach may be explored by encoding locally in parity. We call P the parity mapping from [Fig.2a], where qubits A/B/C/D hold respectively the occupation modulo 2 of the last 4/3/2/1 fermionic modes. The basis elements from the JW transformation

$$\{|1100\rangle_{ABCD}^{JW}, |0011\rangle_{ABCD}^{JW}\} , \quad (8)$$

are, under the encoding P , represented as

$$\{|0100\rangle_{ABCD}^P, |0001\rangle_{ABCD}^P\} . \quad (9)$$

The doubly-excited state in Eq.(7) transformed from JW to the P encoding is

$$\begin{aligned} |\psi\rangle_{ABCD}^P &= \alpha|0100\rangle_{ABCD}^P + \beta|0001\rangle_{ABCD}^P = \\ &= |00\rangle_{AC}^P \otimes \left(\alpha|10\rangle_{BD}^P + \beta|01\rangle_{BD}^P \right) . \end{aligned} \quad (10)$$

The entangled double-excitation subspace in JW representation involving four qubits from Eq.(7) is effectively reduced to two entangled qubits in Eq.(10) using the P encoding.

B. Single electronic excitation

Although double excitations represent the major source of correlations in electronic structure problems, it is worth investigating the single electronic excitation case, involving the promotion of a single electron. In fact, the resulting state is symmetric in terms of spin, and single excitations may be computed between two molecular orbitals (MOs), involving a total of 4 SOs.

Let's explore this concept further by introducing an idealized scenario that revolves around the excitation subspace in JW representation [Fig.2c]. To better understand this, let's take the state $|1100\rangle_{ABCD}$ and possible single-excitations acting on it symmetrically in terms of spin. The resulting subspace is then spanned by $|1100\rangle_{ABCD}$, $|0110\rangle_{ABCD}$ and $|1001\rangle_{ABCD}$. This implies that the state can be represented as follows:

$$|\psi\rangle_{ABCD}^{JW} = \alpha|1100\rangle_{ABCD}^{JW} + \beta|0110\rangle_{ABCD}^{JW} + \beta|1001\rangle_{ABCD}^{JW} \quad (11)$$

Upon closer examination, the single excitation seems to be more intricate than initially expected, involving entanglement among all four qubits. We can consider again the mapping P from [Fig.2a]. The basis elements

$$\{|1100\rangle_{ABCD}^P, |0110\rangle_{ABCD}^P, |1001\rangle_{ABCD}^P\} , \quad (12)$$

are transformed respectively into

$$\{|0100\rangle_{ABCD}^P, |0010\rangle_{ABCD}^P, |0110\rangle_{ABCD}^P\} . \quad (13)$$

The singly-excited state from Eq.(11) in JW representation, is transformed in the P representation to

$$|\psi\rangle_{ABCD}^P = |00\rangle_{AD}^P \otimes \left(\alpha|10\rangle_{BC}^P + \beta|01\rangle_{BC}^P + \beta|11\rangle_{BC}^P \right) . \quad (14)$$

Most importantly, the requirement of entangling 4 qubits in JW for Eq.(11), is again reduced to 2 qubits in the P encoding for Eq.(14).

Note that we have used a CI-like scenario in the previous example, where a potential single electron excitation acts linear on the initial state $|1100\rangle_{ABCD}^{JW}$. In a typical quantum computing scenario, the single excitations will be introduced via a unitary-coupled cluster type operator (see next section) that will also produce the state $|0011\rangle_{ABCD}^{JW}$ where both single electrons are excited at the same time. The corresponding amplitude will be on the order of $\alpha\beta$, so that the effect of the now imperfect compression under the parity mapping will become negligible for small amplitudes. As single electron excitations can be identified with orbital rotations (see Eq.(12) in [37]) this motivates future combinations with orbital optimization techniques.

In complex quantum-chemistry scenarios with multiple SOs and correlations, the reduced density matrices may exhibit a high degree of mixed states. This arises due to the possibility of multiple excitations affecting the same SOs, thereby introducing complexity in the previously idealized cases, even in an potential orbital optimized variant. Although we are constrained in the number of excitations we can simplify using the aforementioned methods, we can still deal with excitations that contribute the most to correlation effects.

In the upcoming sections, our focus will be on identifying relevant excitations and explore how the entanglement map transforms under the fermion-to-qubit mapping chosen. Our objective is to investigate the potential to mitigate correlations by employing a clever mapping strategy in complex scenarios.

IV. REDUCING ENTANGLEMENT ON SMALL MOLECULAR SYSTEMS

In order to simplify qubit space entanglement as outlined in the previous section, we first proceed identify the primary sources of correlation based on single and/or double excitations. Then, we will replicate the entanglement streamline procedure by locally encoding parity of the fermionic modes associated to the selected excitation(s). For achieving these objectives, the algorithmic steps implemented in this work are detailed in [Alg.1].

For the sake of clarity, we provide a detailed implementation of [Alg.1] along the simple yet illustrative example of *LiH* molecule. We depart from the associated Hartree-Fock uncorrelated reference state $|\psi_{HF}\rangle$, computed in JW encoding [Fig.3a], *STO-3G* basis and a frozen core orbital for *Li* nuclei [Appendix A]. In this scenario, *LiH* system is represented within an active space of 2 electrons, both occupying the lowest energy

MO in the HF state, which corresponds to 5 MOs in total. Our initial objective is to identify the most relevant double excitations. We can achieve this through different means, for instance through the computation of the commutator of corresponding operators with the Hamiltonian, similar to the process used in the Adaptive Derivative-Assembled Pseudo-Trotter (ADAPT) ansatz VQE [38]. However, we proceed by consider the unitary coupled cluster of singles and doubles (UCCSD), consisting in an optimization of the following parameterized state:

$$|\psi_{UCCSD}\rangle = e^{\hat{\mathcal{T}}_1 + \hat{\mathcal{T}}_2} |\psi_{HF}\rangle$$

$$\hat{\mathcal{T}}_1 = \sum_{ia} \theta_{ia} \left(a_a^\dagger a_i - a_i^\dagger a_a \right)$$

$$\hat{\mathcal{T}}_2 = \sum_{ijab} \theta_{ijab} \left(a_a^\dagger a_b^\dagger a_i a_j - a_i^\dagger a_j^\dagger a_a a_b \right) . \quad (15)$$

More specifically, we consider the paired generalized version (UpCCGSD), which only considers double excitations promoting two electrons from two filled modes of the same MO into two other modes of another virtual MO. Additionally, single excitations are only considered between modes of equal spin, being equivalent between different spin orientations of the same MOs. From now on we define respectively the parameterized angles θ_{ij}^s and θ_{ij}^d as the ones involved in the single and double excitations between MOs i and j . Following the UpCCGSD, we can identify relevant excitations by examining the absolute values of the optimized angles $\{|\theta_{ij}^s|\}$ for single [Fig.3b] and $\{|\theta_{ij}^d|\}$ for double [Fig.3c] excitations. Note that in the present case, only the first molecular orbital is initially occupied in the HF state.

In [Fig.3c] it becomes clear that the most critical double-electron excitation involves the promotion of two

Algorithm1 Reduced-entanglement fermion-to-qubit mappings.

Require: A Hartree-Fock $|\psi_{HF}\rangle$ approximation of the target state in JW encoding.

- 1: Compute UpCCGSD optimization over $|\psi_{HF}\rangle$.
- 2: Retrieve the absolute values for the converged angles $\{|\theta_{i,j}^s|, |\theta_{i,j}^d|\}_{i,j}$.
- 3: Select relevant excitation/s with large value/s of $\{|\theta_{i,j}^s|, |\theta_{i,j}^d|\}_{i,j}$, involving modes with relevant electronic occupation.
- 4: For each selected excitation, encode the associated fermionic modes in a x -branch of a TT mapping \mathcal{T} , replicating Eqs.(10, 14).
- 5: Complete \mathcal{T} by encoding the remaining fermionic modes in a z -branch fashion, ideally from the root node.
- 6: **return** A tailored mapping \mathcal{T} having the target state representation with reduced entanglement requirements.

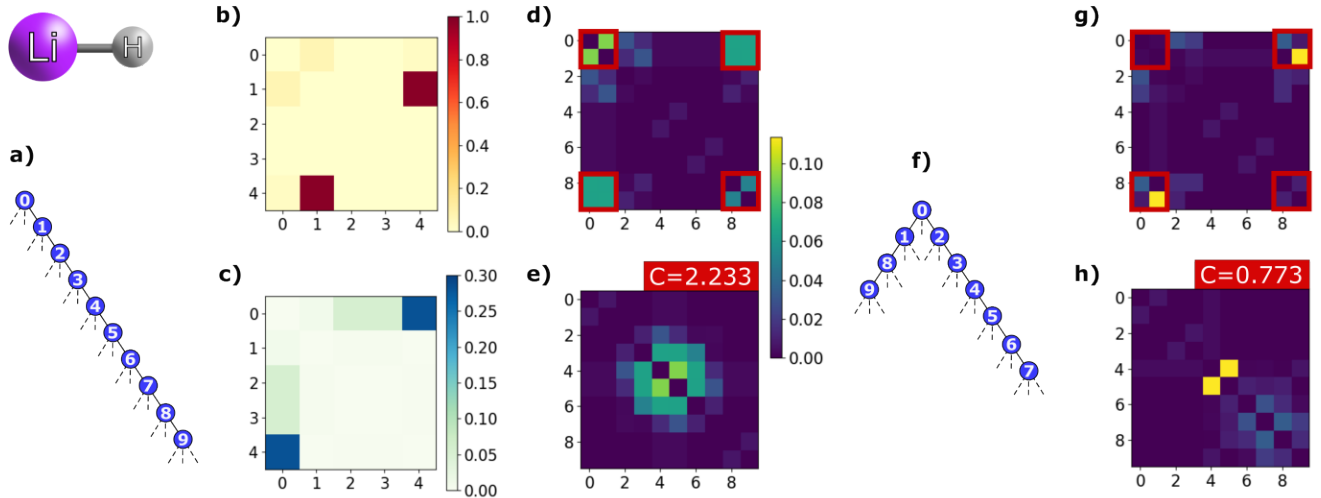


Figure 3. Simplification of LiH entanglement spectrum on a 5 MO active space with 2 electrons. An analysis in the JW encoding is performed in first instance. The gathered information is then used to construct a tailored mapping. **a)** TT corresponding to JW encoding **b)** Absolute values $|\theta_{ij}^s|$ after UpCCGSD, corresponding to single excitations between MOs i and j . **c)** Absolute values $|\theta_{ij}^d|$ after UpCCGSD, corresponding to double excitations between MOs i and j . **d)** Mutual information matrix between SOs for JW ground state. **e)** Mutual information matrix reordered minimizing Eq.(16). **f)** Constructed mapping encoding the most relevant double excitation subspace locally in parity. **g)** Ground state mutual information matrix for the adapted mapping that reduces entanglement on the double excitation between SOs 0,1,2 and 3. **h)** Ground state reordered mutual information matrix for the adapted mapping. Red labels indicate the cost function value of the corresponding mutual information matrices, and red squares indicate the 4 qubits directly involved in the most relevant double excitation.

electrons from the filled MO 0 to the virtual MO 4. While other double excitations (for instance, the ones including virtual MOs 0-2 and 0-3) exhibit importance, they are comparatively less significant. In [Fig.3b], we observe a mild single excitation occurring between MOs 0 and 1. However, it's worth noting that the large absolute angle between MOs 1 and 4, indicative of a potential single excitation, is constructed over other excitations, as both MO remain empty in the HF state. Overall, the double excitation from MO 0 to MO 4 stands as the primary source of correlation, involving SOs and qubits 0, 1, 8, and 9 in the JW encoding scheme.

In this small molecule case, we have the privilege of accessing the exact ground state using exact diagonalization. As part of our analysis, we compute the mutual information (MI) matrix, denoted as I , holding as elements I_{ij} the MI between qubits i and j . This matrix serves as an informative indicator of the entanglement or correlation between SOs i and j [Fig.3d]. An immediate observation reveals the influence of the double excitation between MO 0 and MO 4, as relevant MI is present between associated qubits 0, 1, 8, and 9 (subspace marked in red squares).

To streamline the state preparation process, the extent of long-range entanglement among the qubits can be minimized. This can be done by different means, such as minimizing the long-range MI between subparties [39], or through the exchange matrix [40]. Following the

orbital reordering DMRG approach in the former case, we consider the cost function on our MI matrix

$$C(I) = \sum_{i,j>i} I_{ij} |i - j|^2 , \quad (16)$$

which relates to the Fiedler vector of the MI graph. In essence, the cost function tends to decrease when qubits with substantial MI are positioned closer to each other in a linear order. Considering the set of permutations of n elements $\{P\} \in \mathcal{S}_n$, the permutation P_{opt} is defined as the one that leads to a MI matrix minimizing Eq.(16),

$$P_{opt} = \arg \min_{P \in \mathcal{S}_m} C(PIP^{-1}) . \quad (17)$$

As discussed in section II, it is important to note that permuting physically the qubits doesn't alter the ground state itself but does affect the geometric constraints between subparties, which becomes crucial for upcoming optimization methods. Although finding the exact P_{opt} is hard, it is sufficient a good approximation P_s reducing the cost function from Eq.(16) as much as possible. The search for P_s has demonstrated remarkable benefits in improving VQE simulations, especially on hardware with a linear restricted entangling connectivity [41]. Moreover, DMRG optimization over an MPS has also proven enhanced performance [39]. For the present case, we set P_s as the best solution found along a genetic algorithm using DEAP [42]. The reordered MI matrix associated to P_s significantly reduces the cost function (16), displayed in [Fig.3e].

After identifying qubits 0, 1, 8, 9 as the subparticles involved in the most relevant double excitation of the system [Fig.3c], we proceed to transform the 4-qubit entangled subspace resulting from the double excitation described in Eq.(7) into a 2-qubit entangled subspace, as described in Eq.(10). To do so, we introduce the ternary tree from [Fig.3f]. Such tailored transformation encodes occupation non-locally between the qubits involved in the x -branch (similar to a parity mapping), while occupation remains locally encoded in the qubits from the z -branch (similar to JW mapping).

To visualize the effects of the tailored mapping, we examine the MI matrix of the associated ground state obtained by exact diagonalization [Fig.3g]. Modes A/B/C/D defined in the idealized scenario from Eq.(7), correspond respectively to qubits 0/1/8/9 (marked in red squares). Notably, qubits B (1) and D (9) exhibit significant entanglement in accordance with Eq.(10), as indicated by the mutual information elements $I_{1,9} = I_{9,1}$. While the transformation has simplified the entanglement structure, it is important to remark that not all qubits have been perfectly disentangled. This is due to additional single and double excitations contributing to the overall entanglement. Most importantly, the MI matrix for the new mapping can be now rearranged minimizing the cost function from Eq.(16), yielding [Fig.3h]. When we compare the value of the cost function for the tailored mapping ($C = 0.773$) with that of the JW-reordered matrix ($C = 2.233$), it becomes evident that we have achieved a significant reduction in entanglement requirements by solely focusing on the most critical double excitation.

This methodology has been successfully applied to other small molecular systems [Appendix A]. For H_2 in 6 – 31G basis (4 MO), the procedure has been used to disentangle the 0-1 double excitation. In the case of the highly-correlated H_4 system, which also featured 4 MOs and posed a 4-electron problem, we employed the same approach to simplify the double excitation involving MOs 1 and 2. In the scenario of $(H_2)_2$, we encountered two different double excitations, each involving distinct MOs. To tackle this situation, we introduced a TT encoding scheme with a unique parity x -branch encoding both excitations at the same time.

V. ENHANCING VQE PERFORMANCE

On the considered molecular Hamiltonians, VQE performance has been evaluated for both JW and tailored TT mappings. VQE simulations have been implemented in TEQUILA using the COBYLA optimizer [43] and Qulacs simulator [44].

We compare the lowest VQE energy (E_{VQE}) obtained after 10 VQE executions with the FCI energy

(E_{FCI}), with respect to the number of entangling layers employed in a hardware efficient ansatz (HEA) consisting of RY gates [Fig.4]. The RY-HEA ansatz employed consists of alternating layers of parameterized RY rotations and entangling CNOT gates [Appendix A]. In the figure, the benchmarked data for the JW mapping extracted from [41] is included in red. We conducted a replication of the method using our own hyper-parameters and number of runs. Our results after the 10 VQE optimizations as function of the amount of entangling layers are plotted both for the JW mapping and tailored TT mappings from the previous section.

Overall, the proposed mappings demonstrate superior performance across all studied systems, leading to a faster attainment of chemical accuracy at 1 Kcal/Mol. For LiH , our tailored mapping achieves chemical accuracy with just 4 layers, in contrast to the 8 layers required by the JW mapping. For both H_2 and $(H_2)_2$ cases, the selected mapping achieves accuracy with only 6 layers, whereas JW fails to reach this level of precision even with 10 layers. For the highly-correlated $H_4^{\#}$ system ($E_{HF} - E_{FCI} = 153.640$ Kcal/Mol), chemical accuracy is attained with the tailored mapping using 8 entangling layers, while the JW mapping falls short again when using 10 entangling layers.

The motivation for employing a RY-HEA primitive circuit design is to provide a balanced ground for comparisons between standard and tailored fermion-to-qubit mappings. If compared to targeted circuit designs in JW representation [20], we reach competitive circuit depths (9 vs 12 for LiH ; 17 vs 130 for H_4). Note that by design of the RY-HEA ansatz, this comes with an increased parameter count (46 vs 5 for LiH , 64 vs 10 for H_4) in addition to substantially longer iteration counts. Since the techniques from [20] do not strictly require a JW representation, we estimate significant improvements in combination with the fermion-to-qubit mappings developed in this work.

VI. ENHANCING DMRG PERFORMANCE

The methodology employed in the previous sections has also been adapted in tensor networks, with the goal to improve DMRG optimization on an MPS decomposition using TeNPy [45]. The molecular system of N_2 has been initialized in *STO-3G* basis with 2 core orbitals frozen, resulting in an active space of 16 SOs [Appendix A]. Again, a UpCCGSD optimization has been performed, resulting in converged angles $\{|\theta_{ij}^s|\}$ for single [Fig.5a] and $\{|\theta_{ij}^d|\}$ for double excitations [Fig.5b]. We immediately appreciate the relevant contributions of double excitations between MOs 2-6 and 3-5, and propose a TT mapping encoding such excitations in parity. In this case, we encode each double excitation in a different parity x -branch of the TT, as depicted in [Fig.5c].

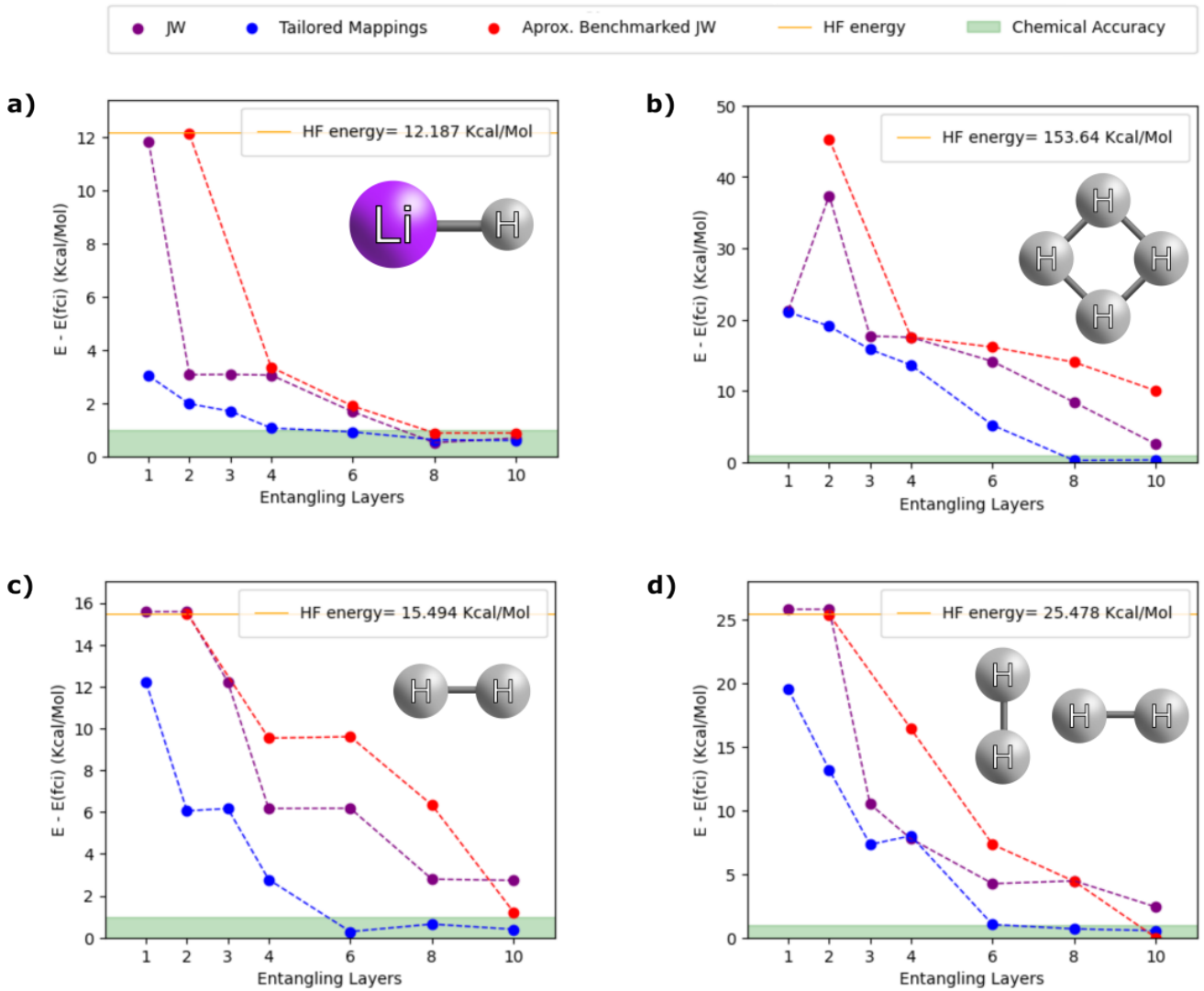


Figure 4. $E_{VQE} - E_{FCI}$ as function of the RY HEA entangling layers for the considered molecular systems a) LiH b) H_4^{\neq} c) H_2 d) $(\text{H}_2)_2$. Comparison of the benchmarked JW reordered (red), JW reordered executed with our optimizers, backends and hyperparameters for fair comparison (purple) and tailored mapping reordered (blue).

Subsequently, a study using DMRG has been undertaken to assess the effectiveness of the proposed mapping. The energy obtained (E_{DMRG}) has been compared to E_{FCI} for different maximum bond dimension cutoffs (χ_{max}), keeping for each bond dimension the best result after 10 optimizations to avoid local minima convergence [Fig.5d]. For the DMRG, an exponentially-decaying mixer has been applied for 30 sweeps, allowing a maximum number of 500 sweeps for the optimization. Several scenarios have been computed to study the dependency on χ_{max} . First, the best JW result is plotted in the standard spin-orbital ordering (red dots). Orbital reordering is then performed by minimizing the cost function from Eq.(16) for the MI matrix, and DMRG is executed again in the optimized order (red circles) [39]. DMRG has also been performed on our tailored mapping (blue dots), and the same reordering

process has been applied to permute the MPS sites and execute DMRG again (blue circles).

An improvement of the DMRG performance is observed using the tailored TT mapping. For a given χ_{max} , the DMRG algorithm achieves lower converged energies, leading to a more accurate simulation of the quantum state. We relate such improvements to the reduced entanglement requirements. A decrease in block entropy is observed for the tailored mapping, both in the cases of standard ordering and reordered systems. This is visualized by studying the block entropy for the best converged MPS at $\chi_{max} = 50$ [Fig.5e]. The final MI matrices for the converged states at $\chi_{max} = 50$ is displayed in [Fig.9] in [Appendix.A].

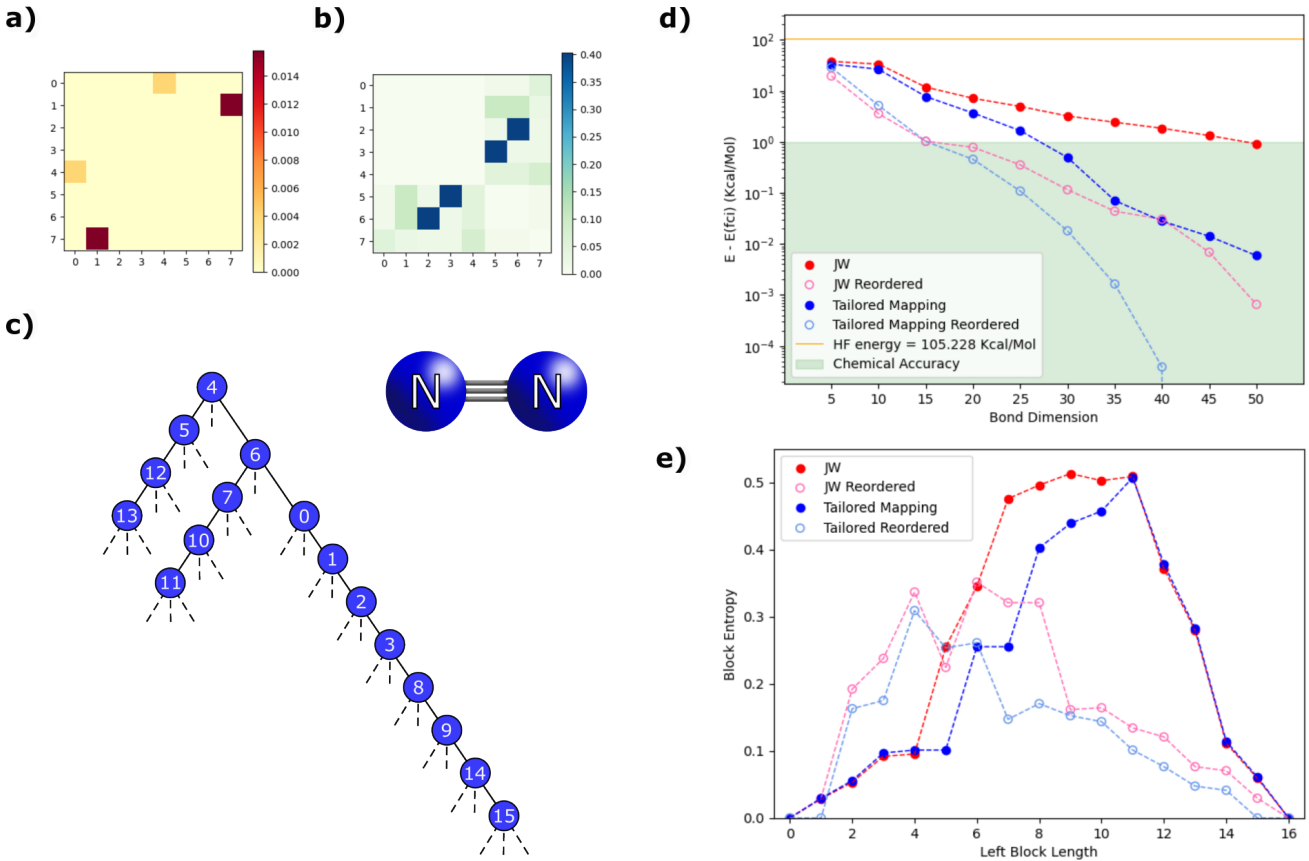


Figure 5. DMRG results for the Nitrogen molecule. **a)** UpCCGSD single excitation angles for JW. **b)** UpCCGSD double excitation angles for JW. **c)** Proposed TT mapping, encoding locally in parity the two double excitation subspaces (4, 5, 12, 13) and (6, 7, 10, 11). **d)** Converged E_{DMRG} energy compared to E_{FCI} as function of the maximum bond dimension used. The proposed TT mapping is compared to the JW mapping. The converged energy for the reordered MPS is also plotted for both mappings. **e)** Block entropies for the converged MPS after DMRG.

VII. OPTIMALITY

The presented algorithm is based on an intuitive understanding of the role of excitations in the generation of correlations in fermion-to-qubit mappings. An enhanced performance is observed in the studied examples, however, it is not expected that our algorithm systematically provides the optimal mapping in terms of resources, say number of layers or bond dimension in the considered quantum and classical variational approaches, needed to obtain a given energy value. For the smaller molecules, we have studied how our construction compares to the rest of possible mappings. In particular, we have iterated over all tree structures, globally optimize over the mutual information using a brute-force search of all permutations and then test the resulting mapping with VQE. For H₂, the tailored mapping used here has an optimal MI cost function of 0.611, versus the 1.28 of the JW map or the 1.92 of the parity map in standard orbital ordering. Of all of the optimized MIs of all tree shapes, our tailored mapping has lower MI than 81% of all mappings. This brute-force search also led

to the discovery of trees with lower MI, however each of these displayed worse performance than the tailored mapping when testing with single and double-layer VQE. Although the general trend was that lower MI correlates to better few-layer VQE performance, it is shown not to be guaranteed. It should be noted that this is a heavily restricted VQE, so perhaps it is not so surprising that random mappings do not suppress the four-body correlations sufficiently in order to be expressible in the < 4 layer VQE.

VIII. CONCLUSIONS

In this study we have introduced a novel physically-inspired perspective in the design of fermion-to-qubit mappings. Previous efforts have predominantly focused on reducing the average Pauli weight or the number of qubits employed, which is undeniably important for quantum simulations. However, by focusing on the

major sources of correlation in the physical problem, we have shown that transformations can be tailored in the qubit space to significantly simplify simulations. We remark that our formalism can be adapted both in classical and quantum computing.

Our work points at several research directions that deserve further investigation. First, it is still left to consider the extension of our results to higher order fermionic excitations, on top of fermionic systems with larger spin number. Another critical aspect to investigate revolves around the correlation-mitigating capabilities of our mappings, when scaling to larger systems. Note also that our method reduces the circuit depth at the cost of increasing the Pauli weight. In the context of noisy VQE, it emerges the question of how advantageous can this trade-off be, which can be

studied in future work. Finally, while our formalism has been applied to electronic structure systems found in quantum chemistry, we anticipate possible adaptations of the method to fermionic systems of different nature, such as those found in nuclear structure or condensed matter simulations.

IX. ACKNOWLEDGEMENTS

We thank Guillermo García Pérez for discussions. This work is supported by the ERC AdG CERQUTE, the Government of Spain (FUNQIP, NextGenerationEU PRTIC17.I1 and Quantum in Spain, Severo Ochoa CEX2019-000910-S), Fundació Cellex, Fundació Mir-Puig, Generalitat de Catalunya (CERCA programme), the AXA Chair in Quantum Information Science, EU project PASQUANS2.

[1] N. S. Blunt et al., Perspective on the Current State-of-the-Art of Quantum Computing for Drug Discovery Applications, *Journal of Chemical Theory and Computation* **18**, 7001 (2022).

[2] Y. Cao, J. Romero and A. Aspuru-Guzik, Potential of quantum computing for drug discovery, *IBM Journal of Research and Development* **62**, 6:1 (2018).

[3] V. von Burg et al., Quantum computing enhanced computational catalysis, *Physical Review Research* **3**, 10.1103/physrevresearch.3.033055 (2021).

[4] V. Lordi and J. M. Nichol, Advances and opportunities in materials science for scalable quantum computing, *MRS Bulletin* **46**, 589–595 (2021).

[5] S. R. White, Density matrix formulation for quantum renormalization groups, *Physical review letters* **69**, 2863 (1992).

[6] U. Schollwöck, The density-matrix renormalization group, *Reviews of Modern Physics* **77**, 259 (2005).

[7] G. K.-L. Chan and S. Sharma, The density matrix renormalization group in quantum chemistry, *Annual review of physical chemistry* **62**, 465 (2011).

[8] A. Baiardi and M. Reiher, The density matrix renormalization group in chemistry and molecular physics: Recent developments and new challenges, *The Journal of Chemical Physics* **152**, 10.1063/1.5129672 (2020).

[9] B. L. Hammond, W. A. Lester Jr and P. J. Reynolds, *Monte Carlo methods in ab initio quantum chemistry* (World Scientific, 1994).

[10] S. B. Bravyi and A. Y. Kitaev, Fermionic Quantum Computation, *Annals of Physics* **298**, 210 (2002).

[11] Z. Jiang, A. Kaley, W. Mruczkiewicz and H. Neven, Optimal fermion-to-qubit mapping via ternary trees with applications to reduced quantum states learning, *Quantum* **4**, 276 (2020).

[12] M. Steudtner and S. Wehner, Fermion-to-qubit mappings with varying resource requirements for quantum simulation, *New Journal of Physics* **20**, 063010 (2018).

[13] F. Verstraete and J. I. Cirac, Mapping local Hamiltonians of fermions to local Hamiltonians of spins, *Journal of Statistical Mechanics: Theory and Experiment* **2005**, P09012 (2005).

[14] C. Derby, J. Klassen, J. Bausch and T. Cubitt, Compact fermion to qubit mappings, *Phys. Rev. B* **104**, 035118 (2021).

[15] R. W. Chien, S. Xue, T. S. Hardikar, K. Setia and J. D. Whitfield, Analysis of superfast encoding performance for electronic structure simulations, *Physical Review A* **100**, 032337 (2019).

[16] R. W. Chien and J. Klassen, Optimizing fermionic encodings for both Hamiltonian and hardware, *arXiv preprint arXiv:2210.05652* (2022).

[17] A. Miller, Z. Zimborás, S. Knecht, S. Maniscalco and G. García-Pérez, Bonsai Algorithm: Grow Your Own Fermion-to-Qubit Mappings, *PRX Quantum* **4**, 030314 (2023).

[18] K. Mitarai, M. Negoro, M. Kitagawa and K. Fujii, Quantum circuit learning, *Physical Review A* **98**, <https://10.1103/physreva.98.032309> (2018).

[19] I. O. Sokolov et al., Quantum orbital-optimized unitary coupled cluster methods in the strongly correlated regime: Can quantum algorithms outperform their classical equivalents?, *The Journal of chemical physics* **152**, 10.1063/1.5141835 (2020).

[20] J. S. Kottmann, Molecular quantum circuit design: A graph-based approach, *Quantum* **7**, 1073 (2023).

[21] M. Motta et al., Quantum simulation of electronic structure with a transcorrelated Hamiltonian: improved accuracy with a smaller footprint on the quantum computer, *Physical Chemistry Chemical Physics* **22**, 24270 (2020).

[22] S. McArdle and D. P. Tew, Improving the accuracy of quantum computational chemistry using the transcorrelated method, *arXiv: Quantum Physics* (2020).

[23] P. Schleich, J. S. Kottmann and A. Aspuru-Guzik, Improving the accuracy of the variational quantum eigensolver for molecular systems by the explicitly-correlated perturbative [2] R12-correction, *Physical Chemistry Chemical Physics* **24**, 13550 (2022).

[24] A. Kumar et al., Quantum Simulation of Molecular Electronic States with a Transcorrelated Hamiltonian: Higher Accuracy with Fewer Qubits, *Journal of Chemical The-*

ory and Computation **18**, 5312 (2022).

[25] I. O. Sokolov, W. Dobrautz, H. Luo, A. Alavi and I. Tavernelli, Orders of magnitude increased accuracy for quantum many-body problems on quantum computers via an exact transcorrelated method, *Physical Review Research* **5**, 023174 (2023).

[26] W. Dobrautz et al., Ab Initio Transcorrelated Method enabling accurate Quantum Chemistry on near-term Quantum Hardware, *arXiv preprint arXiv:2303.02007* 10.48550/arXiv.2303.02007 (2023).

[27] H. Volkmann, R. Sathyaranarayanan, A. Saenz, K. Jansen and S. Kühn, A qubit-ADAPT Implementation for H₂ Molecules using an Explicitly Correlated Basis, *arXiv preprint arXiv:2308.07259* 10.48550/arXiv.2308.07259 (2023).

[28] R. V. Mishmash et al., Hierarchical Clifford Transformations to Reduce Entanglement in Quantum Chemistry Wave Functions, *Journal of Chemical Theory and Computation* **19**, 3194 (2023), pMID: 37227024, <https://doi.org/10.1021/acs.jctc.3c00228>.

[29] P. Schleich et al., Partitioning Quantum Chemistry Simulations with Clifford Circuits, *Journal of Chemical Theory and Computation* **19**, 4952 (2023), pMID: 37490516, <https://doi.org/10.1021/acs.jctc.3c00335>.

[30] Z.-X. Shang, M.-C. Chen, X. Yuan, C.-Y. Lu and J.-W. Pan, Schrödinger-Heisenberg variational quantum algorithms, *Physical Review Letters* **131**, 10.1103/physrevlett.131.060406 (2023).

[31] P. Jordan and E. Wigner, Über das Paulische Äquivalenzverbot, *Zeitschrift für Physik* **47**, 631 (1928).

[32] J. S. Kottmann et al., Tequila: A platform for rapid development of quantum algorithms, *Quantum Science and Technology* **6**, 024009 (2021).

[33] M. Chiew and S. Strelchuk, Discovering optimal fermion-qubit mappings through algorithmic enumeration, *Quantum* **7**, 1145 (2023).

[34] S. R. Langhoff and E. R. Davidson, Configuration interaction calculations on the nitrogen molecule, *International Journal of Quantum Chemistry* **8**, 61 (1974).

[35] R. J. Bartlett and M. Musiał, Coupled-cluster theory in quantum chemistry, *Reviews of Modern Physics* **79**, 291 (2007).

[36] A. Anand et al., A quantum computing view on unitary coupled cluster theory, *Chemical Society Reviews* **51**, 1659 (2022).

[37] J. S. Kottmann and F. Scala, Compact Effective Basis Generation: Insights from Interpretable Circuit Design, *arXiv preprint arXiv:2302.10660* 10.48550/arXiv.2302.10660 (2023).

[38] H. R. Grimsley, S. E. Economou, E. Barnes and N. J. Mayhall, An adaptive variational algorithm for exact molecular simulations on a quantum computer (2019).

[39] G. Barcza, Ö. Legeza, K. H. Marti and M. Reiher, Quantum-information analysis of electronic states of different molecular structures, *Physical Review A* **83**, 012508 (2011).

[40] R. Olivares-Amaya et al., The ab-initio density matrix renormalization group in practice, *The Journal of Chemical Physics* **142**, 034102 (2015), https://pubs.aip.org/aip/jcp/article-pdf/doi/10.1063/1.4905329/14692204/034102_1_online.pdf.

[41] N. V. Tkachenko et al., Correlation-informed permutation of qubits for reducing ansatz depth in the variational quantum eigensolver, *PRX Quantum* **2**, 020337 (2021).

[42] F.-A. Fortin, F.-M. De Rainville, M.-A. Gardner, M. Parizeau and C. Gagné, DEAP: Evolutionary Algorithms Made Easy, *Journal of Machine Learning Research* **13**, 2171 (2012).

[43] M. J. Powell, A view of algorithms for optimization without derivatives, *Mathematics Today-Bulletin of the Institute of Mathematics and its Applications* **43**, 170 (2007).

[44] Y. Suzuki et al., Qulacs: a fast and versatile quantum circuit simulator for research purpose, *Quantum* **5**, 559 (2021).

[45] J. Hauschild and F. Pollmann, Efficient numerical simulations with tensor networks: Tensor Network Python (TeNPy), *SciPost Physics Lecture Notes* , 005 (2018).

Appendix A: Supplementary Information

Algorithm2 Pairing algorithm for Majorana strings from a Ternary Tree. Adapted from [17].

Require: A ternary Tree $\mathcal{T} = (V, E)$.

```

1: for  $v_i \in V$  do
2:   if  $v_i^x$  is None then            $\triangleright$  Construction of  $S_i^x$ 
3:     Define  $l$  as the  $x$ -downward leg from  $v_i$ 
4:      $S_i^x \equiv S_l$ 
5:   else
6:      $s = v_i^x$ 
7:     while  $s^z$  is not None do
8:        $s = s^z$ 
9:     Define  $l$  as the  $z$ -downward leg from  $s$ 
10:     $S_i^x \equiv S_l$ 
11:   if  $v_i^y$  is None then            $\triangleright$  Construction of  $S_i^y$ 
12:     Define  $l$  as the  $y$ -downward leg from  $v_i$ 
13:      $S_i^y \equiv S_l$ 
14:   else
15:      $u = v_i^y$ 
16:     while  $u^z$  is not None do
17:        $u = u^z$ 
18:     Define  $l$  as the  $z$ -downward leg from  $u$ 
19:      $S_i^y \equiv S_l$ 
20: return  $\{S_i^x, S_i^y\}_i$        $\triangleright$  Paired majoranas of all nodes  $v_i$ 

```

| Molecule | Basis | Frozen Orbitals | $E^{corr.}(Kcal/Mol)$ | Cartesian Geometry (Å) |
|--------------|----------|-----------------|-----------------------|---|
| H_2 | $6-31G$ | 0 | 15.4945 | H 0.0000 0.0000 -0.3650 H 0.0000 0.0000 0.3641 |
| LiH | $STO-3G$ | 1 | 12.1869 | Li 0.0000 0.0000 0.0000 H 0.0000 0.0000 1.5472 |
| $(H_2)_2$ | $STO-3G$ | 0 | 25.4776 | H 0.0000 0.3674 -2.1264 H 0.0000 -0.3674 -2.1264 H 0.0000 0.0000 1.7590 H 0.0000 0.0000 2.4939 |
| H_4^{\neq} | $STO-3G$ | 0 | 153.6310 | H 0.0000 0.0000 0.7921 H 0.7921 0.0000 0.0000 H 0.0000 0.0000 -0.7921 H -0.7921 0.0000 0.0000 |
| N_2 | $STO-3G$ | 2 | 105.2284 | N 0.0000 0.0000 -0.5669 N 0.0000 0.0000 0.5669 |

Table I. Initialization of molecular systems, including their nuclei cartesian geometry, basis set, number of core orbitals frozen and correlation energy.

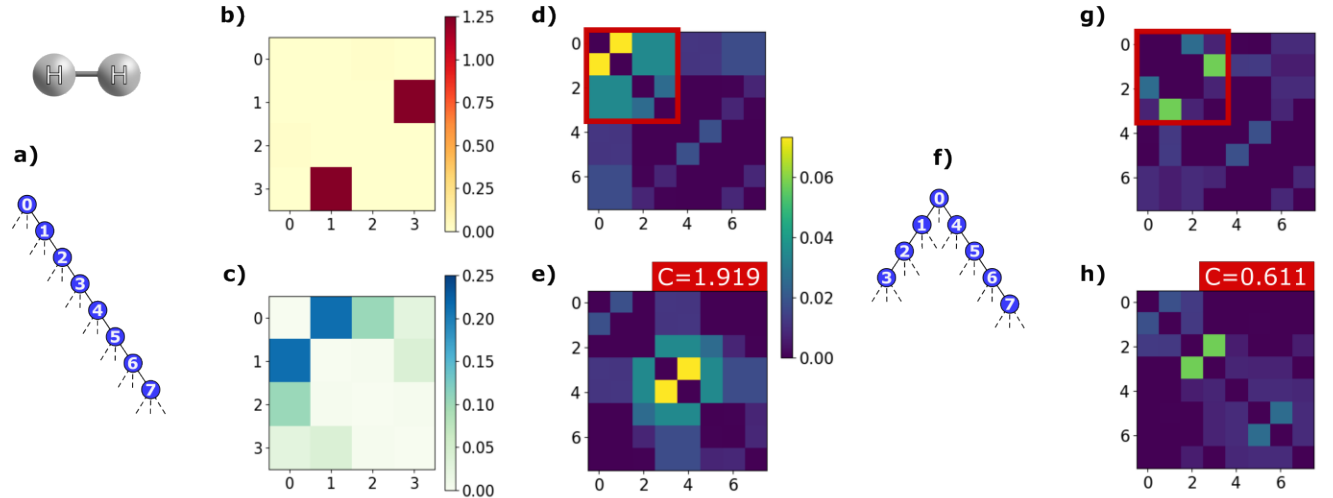


Figure 6. Entanglement reduction process for H_2 . Analogous to the LiH case in [Fig.3]. **a)** JW mapping. **b)** Absolute values $|\theta_{ij}^s|$ after UpCCGSD. **c)** Absolute values $|\theta_{ij}^d|$ after UpCCGSD. **d)** MI matrix between SOs for JW ground state. SOs involved in the most relevant double excitation are marked in the red square. **e)** Reordered JW MI matrix minimizing Eq.(16). Cost is indicated in red. **f)** Tailored mapping proposed from the excitation analysis. **g)** Ground state MI matrix for the tailored mapping that simplifies entanglement on the qubits involved in the relevant double excitation (marked in the red square). **h)** Ground state reordered MI matrix for the tailored mapping. The cost function is indicated in the red labels.

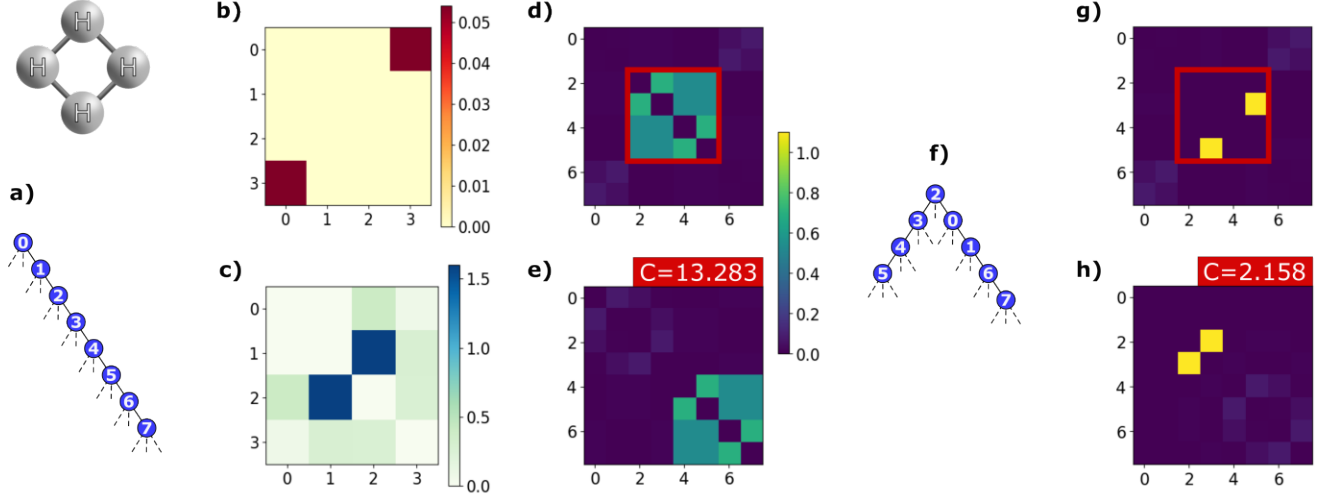


Figure 7. Entanglement reduction process for H_4^{\neq} . Analogous to the LiH case in [Fig.3]. **a)** JW mapping. **b)** Absolute values $|\theta_{ij}^s|$ after UpCCGSD. **c)** Absolute values $|\theta_{ij}^d|$ after UpCCGSD. **d)** MI matrix between SOs for JW ground state. SOs involved in the most relevant double excitation are marked in the red square. **e)** Reordered JW MI matrix minimizing Eq.(16). Cost is indicated in red. **f)** Tailored mapping proposed from the excitation analysis. **g)** Ground state MI matrix for the tailored mapping that simplifies entanglement on the qubits involved in the relevant double excitation (marked in the red square). **h)** Ground state reordered MI matrix for the tailored mapping. The cost function is indicated in the red labels.

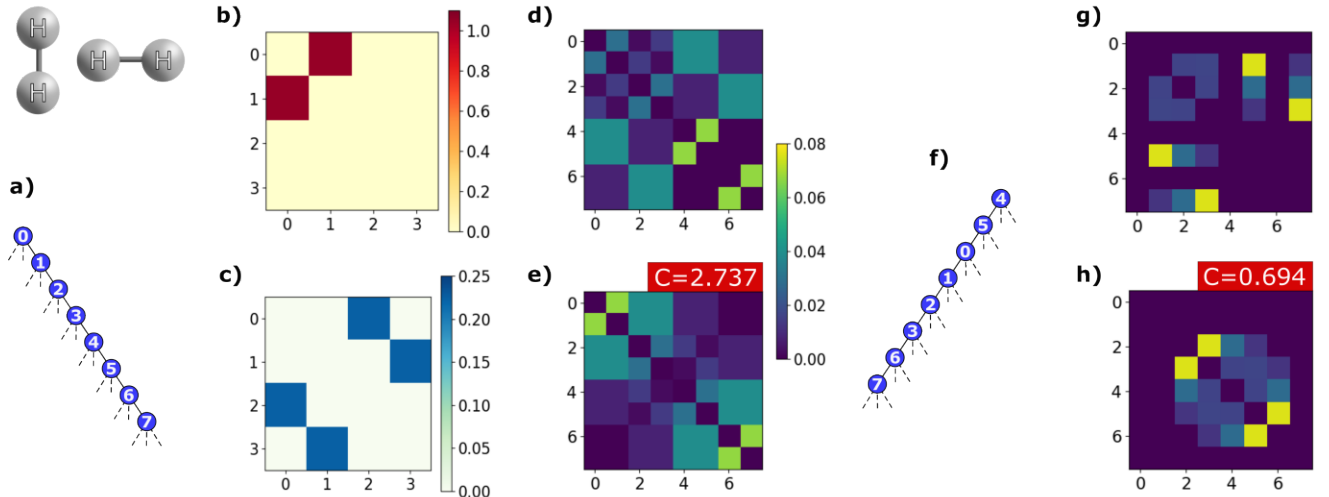


Figure 8. Entanglement reduction process for $(H_2)_2$. Analogous to the LiH case in [Fig.3]. **a)** JW mapping. **b)** Absolute values $|\theta_{ij}^s|$ after UpCCGSD. **c)** Absolute values $|\theta_{ij}^d|$ after UpCCGSD. **d)** MI matrix between SOs for JW ground state. SOs involved in the most relevant double excitation are marked in the red square. **e)** Reordered JW MI matrix minimizing Eq.(16). Cost is indicated in red. **f)** Tailored mapping proposed from the excitation analysis. Note that the two double excitations involving SOs (0,1,4,5) and (2,3,6,7) are included contiguously in the resulting parity order, on top of the (0,1,2,3) SOs involved in the single excitation. **g)** Ground state MI matrix for the tailored mapping that simplifies entanglement on the qubits involved in the relevant double excitation (marked in the red square). **h)** Ground state reordered MI matrix for the tailored mapping. The cost function is indicated in the red labels.

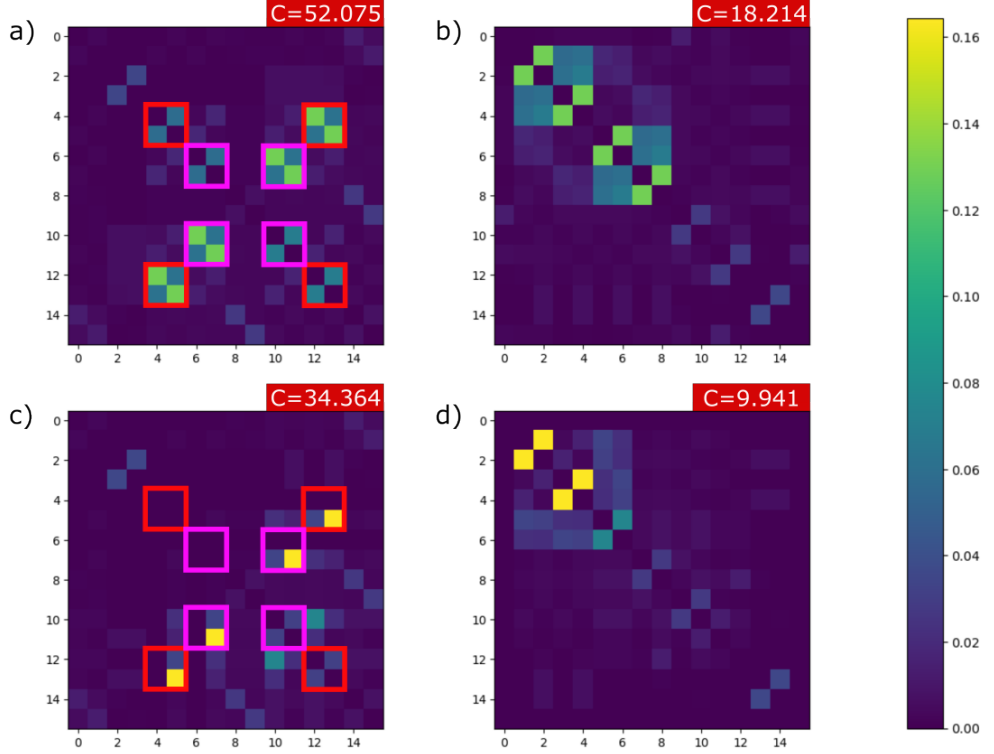


Figure 9. N2 MI matrices for the converged MPS after DMRG for maximum bond dimension 50 in [Fig.5]. The cost function values are indicated in the red labels. The qubits involved in the two relevant double excitations are marked in red and pink squares. **a)** JW encoding. **b)** JW reordered. **c)** Constructed mapping after excitation analysis in [Fig.5c]. **d)** The same constructed mapping reordered.

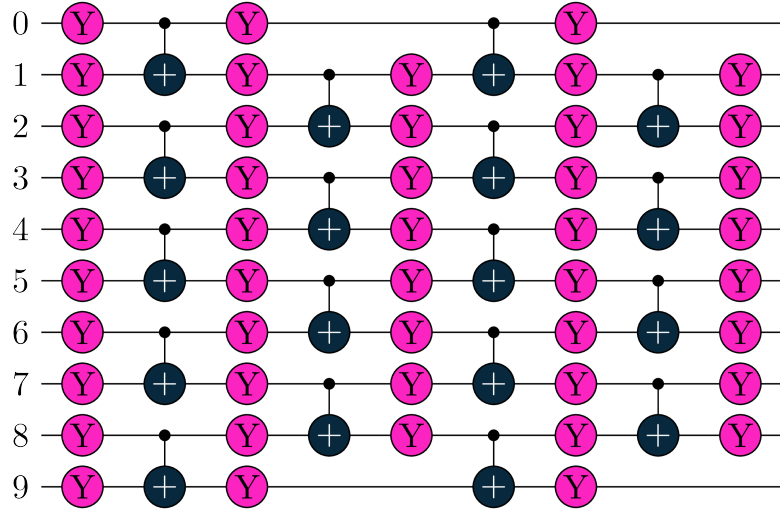


Figure 10. Example of parameterized RY-HEA ansatz of 4 entangling layers, assembled from parameterized R_y rotations and static CNOTs, used for the VQE optimization.

| Label | Pauli String | Ternary Tree |
|----------|---------------|--------------|
| S_0 | $X_0 Z_1 Z_6$ | |
| S_1 | $Y_0 Z_2 Z_7$ | |
| S_2 | $X_0 X_1 Z_4$ | |
| S_3 | $X_0 Y_1 Z_5$ | |
| S_4 | $Y_0 X_2$ | |
| S_5 | $Y_0 Y_2$ | |
| S_6 | $Z_0 X_3$ | |
| S_7 | $Z_0 Y_3 Z_8$ | |
| S_8 | $X_0 X_1 X_4$ | |
| S_9 | $X_0 X_1 Y_4$ | |
| S_{10} | $X_0 Y_1 X_5$ | |
| S_{11} | $X_0 Y_1 Y_5$ | |
| S_{12} | $X_0 Z_1 X_6$ | |
| S_{13} | $X_0 Z_1 Y_6$ | |
| S_{14} | $Y_0 Z_2 X_7$ | |
| S_{15} | $Y_0 Z_2 Y_7$ | |
| S_{16} | $Z_0 Y_3 X_8$ | |
| S_{17} | $Z_0 Y_3 Y_8$ | |
| S_{18} | $Z_0 Z_3 X_9$ | |
| S_{19} | $Z_0 Z_3 Y_9$ | |
| S_{20} | $Z_0 Z_3 Z_9$ | |

Table II. Explicit Pauli strings from the ternary tree in [Fig.1].